

Whole-Brain Multimodal Neuroimaging Model Using Serotonin Receptor Maps Explains Non-linear Functional Effects of LSD

Highlights

- Causal whole-brain model integrating neurotransmitter data and brain dynamics
- This explains the functional effects of serotonin 2A receptor stimulation with LSD
- Non-linear effects of *specific* brainwide distribution of neurotransmitter density
- Exciting possibilities for drug discovery and design in neuropsychiatric disorders

Authors

Gustavo Deco, Josephine Cruzat,
Joana Cabral, ..., Peter C. Whybrow,
Nikos K. Logothetis,
Morten L. Kringelbach

Correspondence

gustavo.deco@upf.edu (G.D.),
morten.kringelbach@psych.ox.ac.uk
(M.L.K.)

In Brief

Deco et al. combined multimodal imaging (dMRI, fMRI, and PET) in a causal whole-brain model to explain the functional effects of 5-HT_{2A}R with LSD in healthy humans. The model identifies the mechanisms for non-linear interactions between the neuronal and neurotransmitter systems and could be used for drug discovery in neuropsychiatric disorders.



Whole-Brain Multimodal Neuroimaging Model Using Serotonin Receptor Maps Explains Non-linear Functional Effects of LSD

Gustavo Deco,^{1,2,3,4,*} Josephine Cruzat,¹ Joana Cabral,^{5,6,7} Gitte M. Knudsen,^{8,9} Robin L. Carhart-Harris,¹⁰ Peter C. Whybrow,¹¹ Nikos K. Logothetis,^{12,13} and Morten L. Kringelbach^{5,6,7,14,15,*}

¹Center for Brain and Cognition, Computational Neuroscience Group, Department of Information and Communication Technologies, Universitat Pompeu Fabra, Roc Boronat 138, 08018 Barcelona, Spain

²Institució Catalana de la Recerca i Estudis Avançats (ICREA), Passeig Lluís Companys 23, 08010 Barcelona, Spain

³Department of Neuropsychology, Max Planck Institute for Human Cognitive and Brain Sciences, 04103 Leipzig, Germany

⁴School of Psychological Sciences, Monash University, Melbourne, Clayton VIC 3800, Australia

⁵Department of Psychiatry, University of Oxford, Oxford, UK

⁶Center for Music in the Brain, Department of Clinical Medicine, Aarhus University, Aarhus, Denmark

⁷Life and Health Sciences Research Institute (ICVS), School of Medicine, University of Minho, 4710-057 Braga, Portugal

⁸Neurobiology Research Unit and Center for Integrated Molecular Brain Imaging, Rigshospitalet, Copenhagen, Denmark

⁹Faculty of Health and Medical Sciences, Copenhagen University, DK-2100 Copenhagen, Denmark

¹⁰Psychedelic Research Group, Centre for Psychiatry, Division of Brain Sciences, Imperial College London, London, UK

¹¹Semel Institute for Neuroscience and Human Behavior, University of California, Los Angeles, Los Angeles, CA, USA

¹²Max Planck Institute for Biological Cybernetics, 72076 Tübingen, Germany

¹³Imaging Science and Biomedical Engineering, University of Manchester, Manchester M13 9PT, UK

¹⁴Institut d'études avancées de Paris, Paris, France

¹⁵Lead Contact

*Correspondence: gustavo.deco@upf.edu (G.D.), morten.kringelbach@psych.ox.ac.uk (M.L.K.)

<https://doi.org/10.1016/j.cub.2018.07.083>

SUMMARY

Understanding the underlying mechanisms of the human brain in health and disease will require models with necessary and sufficient details to explain how function emerges from the underlying anatomy and is shaped by neuromodulation. Here, we provide such a detailed causal explanation using a whole-brain model integrating multimodal imaging in healthy human participants undergoing manipulation of the serotonin system. Specifically, we combined anatomical data from diffusion magnetic resonance imaging (dMRI) and functional magnetic resonance imaging (fMRI) with neurotransmitter data obtained with positron emission tomography (PET) of the detailed serotonin 2A receptor ($5\text{-HT}_{2\text{A}}\text{R}$) density map. This allowed us to model the resting state (with and without concurrent music listening) and mechanistically explain the functional effects of $5\text{-HT}_{2\text{A}}\text{R}$ stimulation with lysergic acid diethylamide (LSD) on healthy participants. The whole-brain model used a dynamical mean-field quantitative description of populations of excitatory and inhibitory neurons as well as the associated synaptic dynamics, where the neuronal gain function of the model is modulated by the $5\text{-HT}_{2\text{A}}\text{R}$ density. The model identified the causative mechanisms for the non-linear interactions between the neuronal and neurotransmitter system, which are uniquely linked to (1) the underlying

anatomical connectivity, (2) the modulation by the specific brainwide distribution of neurotransmitter receptor density, and (3) the non-linear interactions between the two. Taking neuromodulatory activity into account when modeling global brain dynamics will lead to novel insights into human brain function in health and disease and opens exciting possibilities for drug discovery and design in neuropsychiatric disorders.

INTRODUCTION

Human brain activity results from the self-organization of large neural networks, emerging from complex recursive non-linear interactions between interconnected neural populations [1–3]. Understanding brain function and dysfunction clearly requires measurements of such activity in various spatiotemporal scales, some of which may be done by combining neurophysiological and neuroimaging methods, including electrical measurements, fMRI, dMRI (diffusion MRI), and PET (positron emission tomography) [4, 5]. Moreover, modeling of such large-scale brain dynamics is absolutely essential for gaining insights into the generative mechanisms of ongoing neuronal dynamics [6, 7].

Not surprisingly, following the development and optimization of various methodologies over the last 2 decades, significant progress has been made in measuring the spontaneous spatiotemporal unfolding of brain activity, revealing a repertoire of what is currently called resting-state networks [8–10]. In parallel, the spatial patterns of correlated activity in such networks have been increasingly studied with a variety of computational



methods, including whole-brain models relying on the mean activity and variance of excitatory and inhibitory neuronal populations [1, 3, 6, 11–14].

However, the explanatory and potentially predictive power of neuronal population models, such as those of neural mass and mean field, strongly depend on the integration of information that may selectively and differentially affect the activity of populations at different spatial scales [5]. More specifically, whole-brain models commonly rely on structural and functional connectivity of a number of anatomically defined brain regions, the activity of each of which is described by the estimated mean activity of local neuronal populations. Yet, it is now well established that such activity is strongly modulated by the synergistic interactions of the diffuse ascending systems, spreading in a global or local fashion by so-called neuromodulators, including acetylcholine, various monoamines, and tryptamines [15–17]. The effects of these neuromodulators go well beyond the activity profiles of typical excitation-inhibition microcircuits and could only be computationally assessed by having detailed maps of regional density of their receptors.

To address this important problem, we combine standard anatomical and functional maps of the human brain with a detailed map of 5-HT_{2A} receptor (5-HT_{2A}R) density of the neuromodulator serotonin, obtained from a new high-resolution human brain *in vivo* atlas [18], recently composed on the basis of images from 210 healthy individuals (see details of radiotracers in [18]). We added the receptor maps to the standard whole-brain model by investigating how gain values can be adapted by the local regional values of the PET-based empirical values of 5-HT_{2A}R density. To this end, we defined a global gain scaling parameter, s_E , which was added to the original fixed gain parameters (which were the same for all regions) and thus scaling the regional 5-HT_{2A}R values influencing the recursive circuits of excitatory and inhibitory neurons. We first fitted the model to the placebo condition but *not* the LSD condition, i.e., assuming zero values of s_E that correspond to the original gain values. The main question then becomes whether any s_E values would fit the LSD condition (using the sensitivity of the functional connectivity dynamics) while still using the original whole-brain placebo model but now including the new element of receptor binding through the global gain scaling parameter, which modulates each region with the different empirical measures of 5-HT_{2A}R binding. If this were found to be true, neurotransmitter modulation of whole-brain activity dynamics would be—for the first time—quantitatively ascribed to one type of receptor binding (here 5-HT_{2A}) that would be modulating brainwide neural responses.

RESULTS

The main aim is to provide a detailed mechanistic explanation of how neuromodulation is coupled with the neuronal system and serves to shape how function emerges from the underlying anatomy. Here, we describe the results of using a whole-brain model, integrating a whole-brain density map of the 5-HT_{2A}R [18] with traditional structural and functional connectivity representations obtained by means of dMRI and fMRI, respectively. The combination of the multimodal data in the whole-brain model is described in schematized form in Figure 1. Notably, the model

only uses two parameters: a neuronal parameter scaling the global coupling of neuronal populations and a neuromodulator parameter scaling the effects of neurotransmitter on the neuronal gain function weighted by the empirical regional receptor density. For each of the multimodal neuroimaging modalities, we used the automated anatomical labeling (AAL) parcellation with 90 cortical and subcortical regions [19], which has been extensively and successfully used over the last decade for resting-state neuroimaging studies and whole-brain modeling.

We investigated the influence of neuromodulation on the neuronal system using the well-known effects of LSD on the serotonin system by using data obtained in healthy participants receiving small doses of LSD or placebo, with or without music, which can acutely induce synesthesia, altered perceptions, bliss, depersonalization, and mystical experiences [20]. Importantly, LSD with music has been found to enhance the emotional response and produced greater feelings of wonder and transcendence compared with listening to music after placebo [21]. We therefore used the music conditions with placebo and LSD in order to increase the impact on the serotonin system (see Figure 3, and we also confirmed the results for the non-music condition [Figure S1]).

Specifically, the model was first fitted to the placebo condition, and subsequently, the regional 5-HT_{2A}R densities from the *in vivo* atlas were used to explain the functional resting-state activity in the LSD condition. The role of the empirical 5-HT_{2A}R was ultimately assessed by comparing the LSD maps with neuromodulatory maps of randomly shuffled 5-HT_{2A}R densities. As shown below, we found that a robust explanation of global activity changes induced by the LSD administration is only possible when the neuromodulation profiles estimated by the density of the 5-HT_{2A}Rs from the *in vivo* serotonin atlas is taken into account.

Briefly summarizing the methods (full details can be found in the [STAR Methods](#)), the whole-brain model was composed of 90 anatomically delineated brain regions linked by the structural connectivity (SC) matrix of fiber densities obtained by tractography [23, 24]. The activity of each region was represented by a dynamic neuronal mean-field model derived from the collective behavior of empirically validated integrate-and-fire (80% excitatory and 20% inhibitory) neurons [25, 26]. The population responses for pools of excitatory neurons were given by independent sigmoid functions, regulated by a gain parameter s_E , common in all brain regions and initially set to zero (see [STAR Methods](#) and [25]). In the model, the inter-regional coupling (given by the SC) was scaled by a single global parameter, G, corresponding to the conductivity of each fiber (same for all fibers). Modulation of the brain's dynamic working point, i.e., changes in the magnitude of coupling of the network (from weak to strong), could be implemented by changing the G parameter.

Explaining the Influence of Neuromodulation

Our optimization of the whole-brain model on the basis of the aforementioned diverse structural, functional, and regulatory data started with the fitting of the whole-brain mean-field model to the placebo condition, using the same fixed gain-value parameters for all regions and adapting only the G coupling parameter. This optimal global coupling parameter value was subsequently used for explaining the LSD condition by selectively changing the

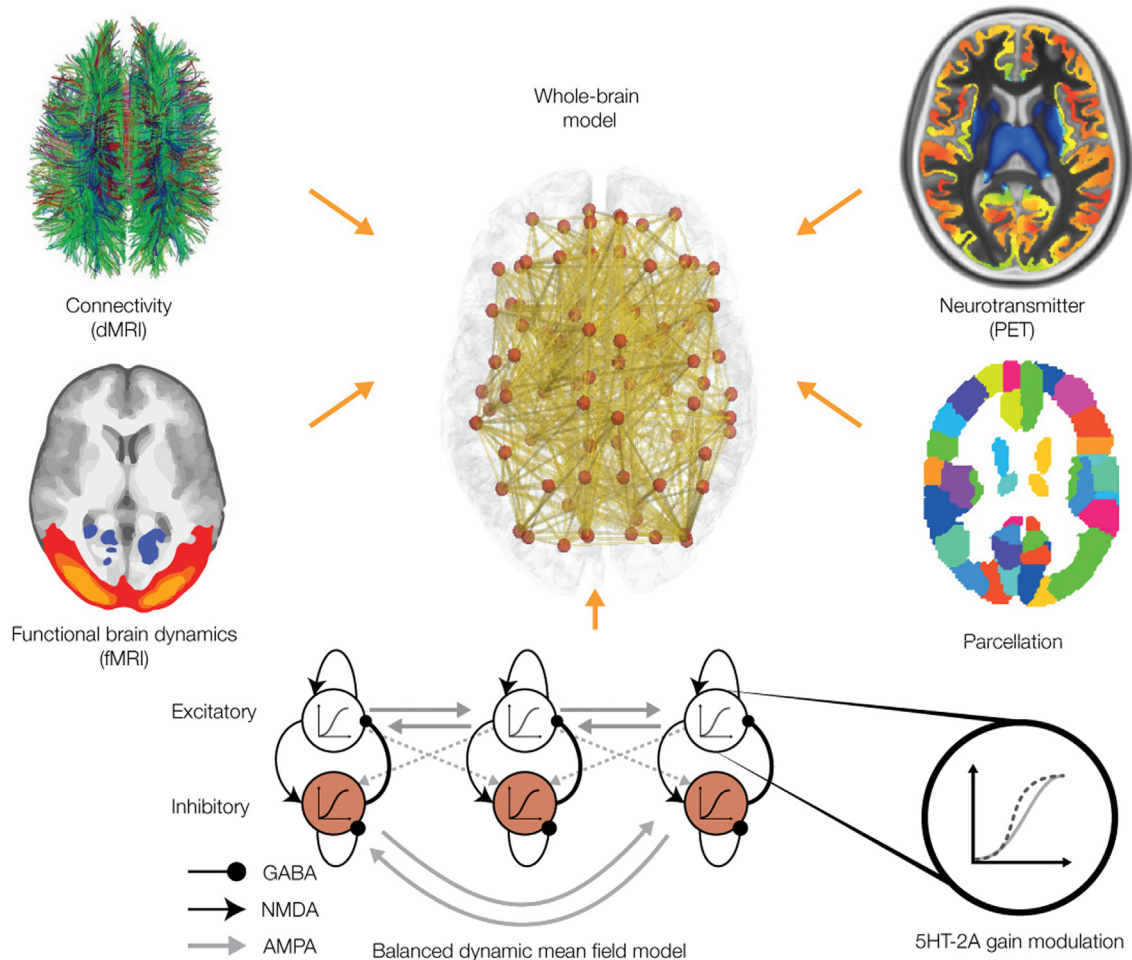


Figure 1. Overview of Integrating Multimodal Data Including Neuromodulation into a Whole-Brain Neuronal Model

We show the basic ingredients for the integration of multimodal neuroimaging data from structural (dMRI, top left), functional (fMRI, bottom left), and neurotransmission (PET, top right) using the same parcellation for each neuroimaging modality (bottom right) for generating a whole-brain computational model (middle). Each node of the model is using a realistic underlying biophysical neuronal model including AMPA, GABA, and NMDA synapses as well as neurotransmitter gain modulation (bottom row) of these.

neuronal gain of each region according to the empirical measured 5-HT_{2A}R density. To take into account the spatiotemporal fluctuations in functional brain dynamics over time, the model was fitted to the spatiotemporal dynamics of the data (i.e., to the functional connectivity dynamics [FCD]) [27–29] rather than to the static grand-average functional connectivity [30] (see Figure 2, describing the process of estimating and fitting the FCD in the whole-brain model). As previously shown, the FCD is a powerful sensitive measure of the spatiotemporal changes in functional connectivity, which maximally constrains the working space parameters of whole-brain models [27, 31]. For this reason, the sensitivity of the FCD offers an excellent metric for determining subtle differences.

Importantly, the gain values were adapted by taking into account the local regional values of 5-HT_{2A}R density (see STAR Methods). Specifically, we defined a global gain-scaling parameter, s_E , which was added to the original fixed gain parameters (same for all regions) and thus could serve for scaling of the regional 5-HT_{2A} values, potentially signaling the influence of the

receptors on the recursive circuits of excitatory and inhibitory neurons. Zero values of s_E yield the original gain values, fitting the model to the placebo condition but *not* the LSD condition. An important subsequent question is whether any s_E values would fit the LSD condition (using the sensitivity of the FCD measure) while still using the optimal coupling G parameter of the placebo condition. If this were true, LSD-induced whole-brain activity dynamics would be quantitatively ascribed to one type (i.e., 5-HT_{2A}) of serotonergic modulation of brainwide neural responses.

Results of Fitting Whole-Brain Neuromodulation Model to Empirical Data

To find the causal mechanisms linking neuromodulation and neuronal activity, we first estimated the optimal coupling parameter G such that the whole-brain model (with original gain values, i.e., $s_E = 0$ for all regions) optimally fits the placebo condition. Figure 3A shows the dependency for G of the fitting in terms of (1) the grand-average static functional connectivity (FC) and (2)

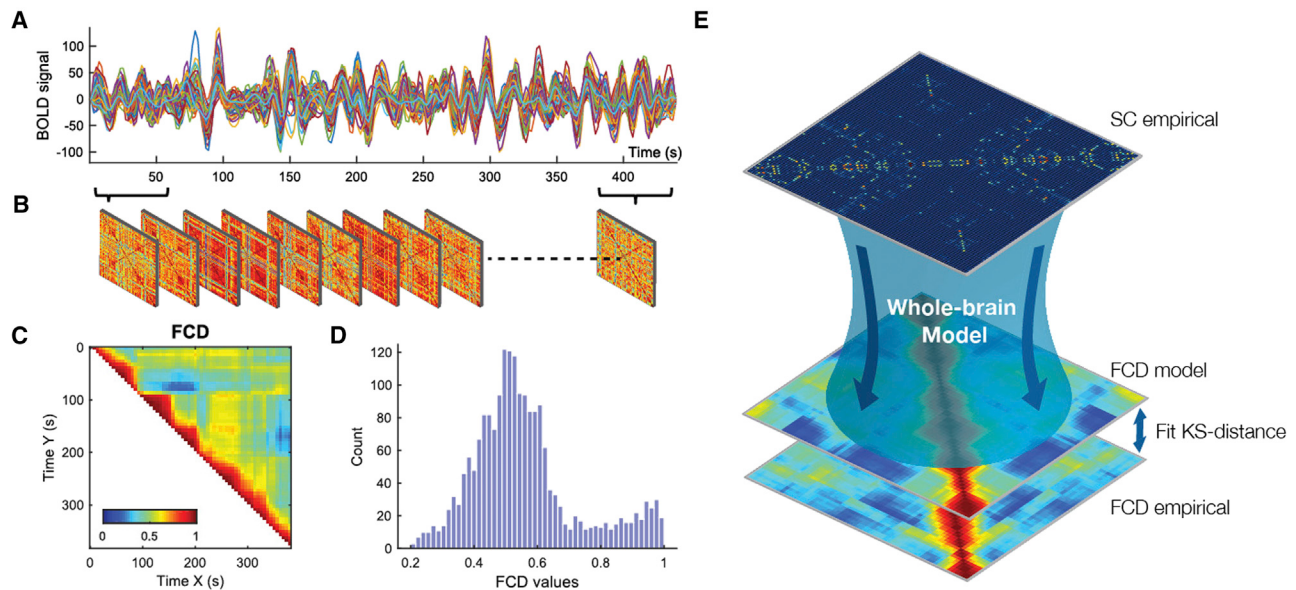


Figure 2. Overview of Process for Estimating and Fitting the FCD in the Whole-Brain Model

- (A) First, we extract the timeseries from the fMRI data from each brain region in the parcellation (shown here for a single participant).
- (B) The average functional connectivity is computed over a sliding window of 30 repetition time (TR) with increments of 2 TR, resulting in time-evolving FC matrices.
- (C) Subsequently, we compute a time-versus-time matrix of FCD, where each entry, $FCD(t_x, t_y)$, corresponds to the correlation between the FC centered at times t_x and the FC centered at t_y .
- (D) We generate the distributions of the upper triangular elements of the FCD matrices over all participants in a given condition (LSD or placebo) and here show the histogram for the single participant.
- (E) The distribution of FCD for the placebo condition is used to fit the whole-brain computational model, which is compared using the Kolmogorov-Smirnov distance, allowing for an effective evaluation of the model performance in explaining the changes observed in resting-state FC in dynamical terms.

the FCD. For the FC fitting, higher values indicate a better fit since it reflects a simple correlation between model and empirical data. We include this measure as the grand-average FC spatial correlation has traditionally been used to constrain whole brain, yet it is not particularly sensitive to the spatiotemporal information [27, 31] and thus not relevant for constraining the model here. Instead, we show that a better measure for model fitting is the FCD, which take into account the spatiotemporal information and where lower values indicate a better fit of the Kolmogorov-Smirnov distance between the FCD of the model and empirical data. As is shown in Figures 3A and 3B, the results using this measure (level of fitting) are excellent. For the subsequent analyses, we use this placebo condition for which we selected the optimum point of G, when the model was fitted to the FCD ($G = 2.1$ at minimum of green line in Figure 3A).

The neuromodulatory effects in the LSD condition were then modeled by estimating the neuronal gain function, namely by scaling the parameter s_E and the corresponding regional empirical 5-HT_{2A}R data. Figure 3B shows how this approach significantly changed the fit, revealing an optimal s_E value of approximately 0.2. In contrast, trying to improve the fit with the placebo condition at the optimal coupling point G as a function of changing the PET-based excitatory gain modulation (see STAR Methods) did not show any improvement. There was no optimal gain modulation. Instead the placebo fit to FCD (green line in Figure 3B) decreased monotonically, as can be seen by the green line in Figure 3B. The finding clearly demonstrates

that the brain-activity profiles, induced by the 5-HT_{2A}R agonist LSD (as fitted to the FCD) depend on the precise 5-HT_{2A}R density distribution map. While we show that this response is non-linear, this finding is consistent with the existing physiological literature revealing a main action of psychedelics such as LSD on the 5-HT_{2A}R [22].

Furthermore, to demonstrate that the LSD function is dependent on the precise distribution of the 5-HT_{2A}R, at the optimal gain value s_E , we randomly shuffled the empirical 5-HT_{2A}R densities; i.e., the original 90 values for the receptor maps were randomly re-assigned to different regions, and the model was run 200 times with each different randomly re-assigned receptor map. Figure 3C shows the results of randomly shuffling the empirical 5-HT_{2A}R densities across the regions at the optimum point s_E (obtained and shown in Figure 3B). This randomly re-shuffled manipulation yields a significantly worse fit compared to the actual empirical receptor densities (as shown by the Wilcoxon statistics in the boxplot).

In order to further test the robustness of our whole-brain modeling approach, we used a number of different strategies to test the specificity of receptor-binding maps. In Figure 3D, we show a boxplot of the results of using a uniform receptor-binding distribution (to the far right). This is significantly worse than all other receptor-binding distributions. We also show the results of using the other serotonin receptors, namely 5-HT_{1A}, 5-HT_{1B}, 5-HT₄, and the serotonin transporter, 5-HTT. These maps all perform significantly worse than that for the 5-HT_{2A}R,

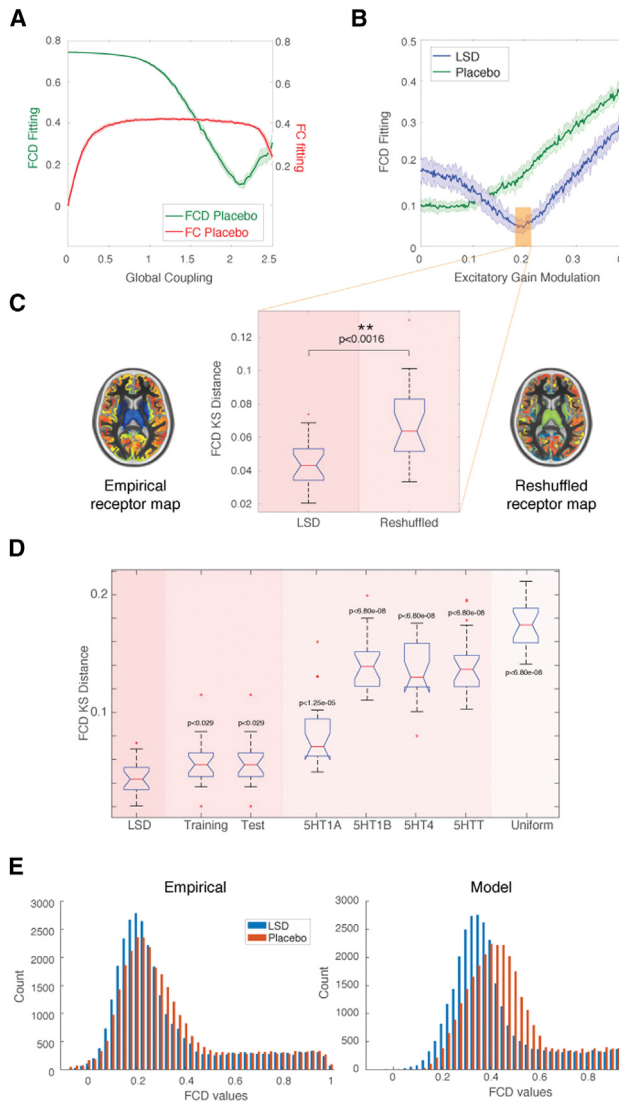


Figure 3. Results of Whole-Brain Model of Placebo and Explaining Effects of LSD with 5HT_{2A} Modulation of Gain Function

(A) Whole-brain fitting of the placebo condition shows the fit of grand average functional connectivity (FC, in red) and functional connectivity dynamics (FCD, in green) as a function of the global coupling parameter, G (with the error bars indicating the standard error across simulations). For the FC fit, higher values indicate a better fit since it reflects a simple correlation between the model and empirical data. However, for the FCD fit, lower values indicate a better fit since we use the Kolmogorov-Smirnov distance between the FCD of the model and empirical data (see STAR Methods for full details). Similar to our previous published research, this shows that the FCD fitting is much more informative than the static grand-average FC, which is to be expected given that FCD provides the functional dynamics. The obtained optimum of G for fitting the model to the FCD (at minimum of green line, $G = 2.1$) is then used for the subsequent neuromodulatory analyses.

(B) For the LSD condition, when using this optimal coupling point of the placebo condition and systematically scaling the excitatory gain function in each region with the empirical 5-HT_{2A}R data, we find that there is an optimum at around (0.2, 0.045) (minimum of blue line). In contrast, varying the scaling of the neuronal gain for the placebo condition does not yield an optimum (see monotonically rising green line), and thus the fit is not improved by changing the scaling of the neuronal gain by 5-HT_{2A}R density. This clearly demonstrates

which confirms the main role this receptor plays in the effects of LSD [22]. It has been suggested that the 5-HT_{1A} receptor also contributes to the effects of LSD [22, 32], and indeed, this is confirmed by the improved performance of the 5-HT_{1A} receptor-binding map compared to the 5-HT_{1B}, 5-HT₄, and 5-HTT maps [22].

We also wanted to test the generalization capability of our model by training and testing the 5-HT_{2A}R maps on a random 50% subset of participants. While our sample was comparably small for a generalization study, we nevertheless were able to show that the training performance was very similar to the original results, while the testing performance was equally good (see Figure 3D).

Further demonstrating the excellent fit, we plot the FCD histograms of LSD and placebo for both the empirical data and the optimized model in Figure 3E, where the histograms of the LSD and placebo conditions are different for both empirical and model. This suggests that the 5-HT_{2A}R density is fundamental for describing the neuromodulatory effects of psychedelics.

DISCUSSION

The findings presented here show for the first time the potential of whole-brain modeling to capture the modulation of brainwide regional activities, typically induced by the ascending neuromodulatory systems that regulate the balance, excitability, and specificity of cortical microcircuits and subcortical neuronal assemblies. We built a novel whole-brain model integrating neuronal and neuromodulation multimodal data from dMRI and fMRI with neurotransmitter data obtained with PET, revealing a detailed whole-brain map of 5-HT_{2A}R densities. This provided new causative insights into the non-linear interactions between anatomy, neuronal activity, and more importantly, specific neurotransmitter receptor density.

Our framework enabled us to model the resting state (with and without music listening) and, more importantly, mechanistically explain the functional effects of 5-HT_{2A}R stimulation with

that the LSD brain activity is dependent on the precise 5-HT_{2A} density distribution maps.

(C) Further, reshuffling the 5-HT_{2A}R densities randomly across the regions at the optimum point in (B), shown within orange box, makes the fit significantly worse ($p < 0.0016$). This again demonstrates that the precise distribution of 5-HT_{2A} is very important for how LSD affects the brain state.

(D) To further test the robustness of our whole-brain modeling approach, we tested the specificity of other receptor-binding maps. Here, we show a boxplot of the results of the generalization capability of our model by training and testing the 5-HT_{2A}R maps on 50% subset of participants (columns 2 and 3). The results are remarkably similar to using the full set of participants, attesting to the robustness of our results. We also show the results of using other serotonin receptor-binding maps, namely 5-HT_{1A}, 5-HT_{1B}, 5-HT₄, and 5-HTT (columns 4–7), which all perform significantly worse than 5-HT_{2A}, confirming the main role this receptor to the effects of LSD [22]. Interestingly, however, 5-HT_{1A} receptor-binding map performs slightly better than the 5-HT_{1B}, 5-HT₄, and 5-HTT receptor maps, which confirms its role in LSD [22]. In the last row, we show the results of using a uniform receptor-binding distribution (column 8), which is significantly worse than all other receptor-binding distributions. (E) Finally, the FCD histograms of LSD and placebo for both the empirical data and the optimized model clearly show the excellent fit. We also confirmed the results for the non-music conditions, as shown in Figure S1.

well-known 5-HT_{2A}R agonist compound LSD in healthy participants. We were able to do so by creating a whole-brain model using the underlying anatomical connectivity linking local nodes, which were modeled using a dynamical mean-field quantitative description of populations of excitatory and inhibitory neurons as well as the associated synaptic dynamics, where the neuronal gain function of the model was modulated by the 5-HT_{2A}R density. As such, we were able to model the non-linear interactions between the underlying anatomical connectivity and the modulation by the specific brainwide distribution of neurotransmitter receptor density.

Importantly, the results were informed by the properties of the serotonin (5-hydroxytryptamine, 5-HT) system, which is a remarkably evolutionary conserved neuromodulator/neurotransmitter that not only regulates psychophysiological functions like sleep, food intake, body temperature, depression/anxiety, alcohol/drug-reinforcement, emotional behavior, environmental sensitivity, and adaptive responsiveness but also modulates cognitive capacities such as learning and memory by interacting with other neuromodulatory and neurotransmitter systems [33–36]. 5-HT is synthesized within the brainstem's raphe nuclei (dorsal and median), which have distributed projections to subcortical, limbic, and neocortical regions [37–39]. On the basis of structural, functional, and transductional features, 5-HT receptors have been grouped into seven receptor groups, including a total of 14 subtypes, and one transporter (5-HTT), which typically transfers a neuromodulator, e.g., serotonin, from the synaptic cleft to the presynaptic neuron [40, 41]. The most abundant and extensively researched subtypes of serotonin receptors are the 5-HT_{1A} and 5-HT_{2A} receptors [36]; the latter has been shown to mediate an adaptive plasticity (i.e., behavioral capacity for change) that is critical for dealing with pathologies, such as stress, adversity, and depression [36]. The hallucinogenic effects of psychedelics such as LSD are mediated through their stimulation of 5-HT_{2A}R [36, 42] (but also to a lesser degree some of the other receptors), and this mode of action may explain the potentially beneficial effects on some of the aforementioned pathologies [43, 44].

The present results extend the recent findings of Shine and colleagues [45] to the human whole-brain level and specially emphasize the role of PET-based binding receptors for global brain dynamics. Until now, it was generally believed that whole-brain dynamics are shaped mainly by the underlying anatomy and the local dynamics. But this is not enough to fully describe the dynamics, as shown by the elegant results of Shine and colleagues emphasizing the role of gain modulation. The present results supplement this work while emphasizing that the incorporation of neuromodulatory properties can significantly add to an account of global functional dynamics. Even more importantly, future research should seek to describe the full entanglement of the two very different neural and neurotransmitter dynamical systems with very different timescales.

Here, neuromodulation was artificially induced by using a serotonin agonist, namely the psychedelic LSD. Yet, the method can be further optimized—potentially by including the receptor distribution of additional neuromodulators—and used for discerning self-generated changes in brain states. Clearly, a

new approach that can reliably describe the evolution of brain states would be of great value both for diagnosis of diseases and drug optimization.

Numerous investigations in human and animals using a great repertoire of non-invasive and invasive techniques has convincingly demonstrated that the functional whole-brain activity depends both on effective connectivity and so-called brain states, reflecting system properties such as anatomical organization, dynamic thalamocortical loops, and the function of ascending arousal systems. Evidently, such evolving activity patterns are affected by diseases and may be eventually used to predict approaching “criticalities,” as the latter transitions are often preceded by robust gradual reorganization of complex systems in general [46].

Further integration of information and modeling is undoubtedly important given the inadequacy of animal models and studies at the microscopic level to fully describe human neuropsychiatric disorders, which have contributed the paucity of effective clinical neuropharmacological interventions such as antidepressants having limited success compared to placebo [47, 48], clearly indicating that new research strategies are needed [49, 50]. In fact, the development and discovery of new effective pharmacological treatments for neuropsychiatric disorders is making incremental progress only, and it has been argued that treatments available today are no more effective than those available over 50 years ago, despite intensive neurobiological investigation [49, 51, 52].

What is needed is a mechanistic understanding of the imbalances found in neuropsychiatric disorders, specifically at both local and global whole-brain levels [4]. This could help open up rational ways for effective brain interventions to rebalance the brain networks and help the identification of biomarkers stratifying a broad illness phenotype into a finite number of treatment-relevant subgroups [53–56].

Neuropsychiatric disorders are bound together by changes on many networks of the brain and in particular in the reward network of the brain [57], with anhedonia, i.e., lack of pleasure, being the cardinal symptom [58]. Systematic studies of changes in local and global neuromodulatory activity, development, optimization and classification of models, and observations of drug effects on them may greatly increase our understanding of pathological states and their potential treatment.

Based on the current findings, we offer here an example of a pipeline (Figure 4) that could potentially be used to combine structural, functional, and neurotransmitter neuroimaging data for modeling a disease state (leftmost). Once the model is established, the regional drug receptor modulation can be optimized by finding the optimal weighting of the receptor density such that the optimized model generates the functional dynamics of the healthy state. The current evidence suggests that it would be important to combine such direct brain manipulations with environmental manipulations, e.g., drug-assisted psychotherapy, which could be a particularly fruitful approach [59].

In summary, we have demonstrated how the anatomical brainwide distribution of neuromodulatory activity can be integrated in a whole-brain computational model to provide new causative insights into the non-linear interactions between anatomy, neuronal activity, and more importantly, *specific*

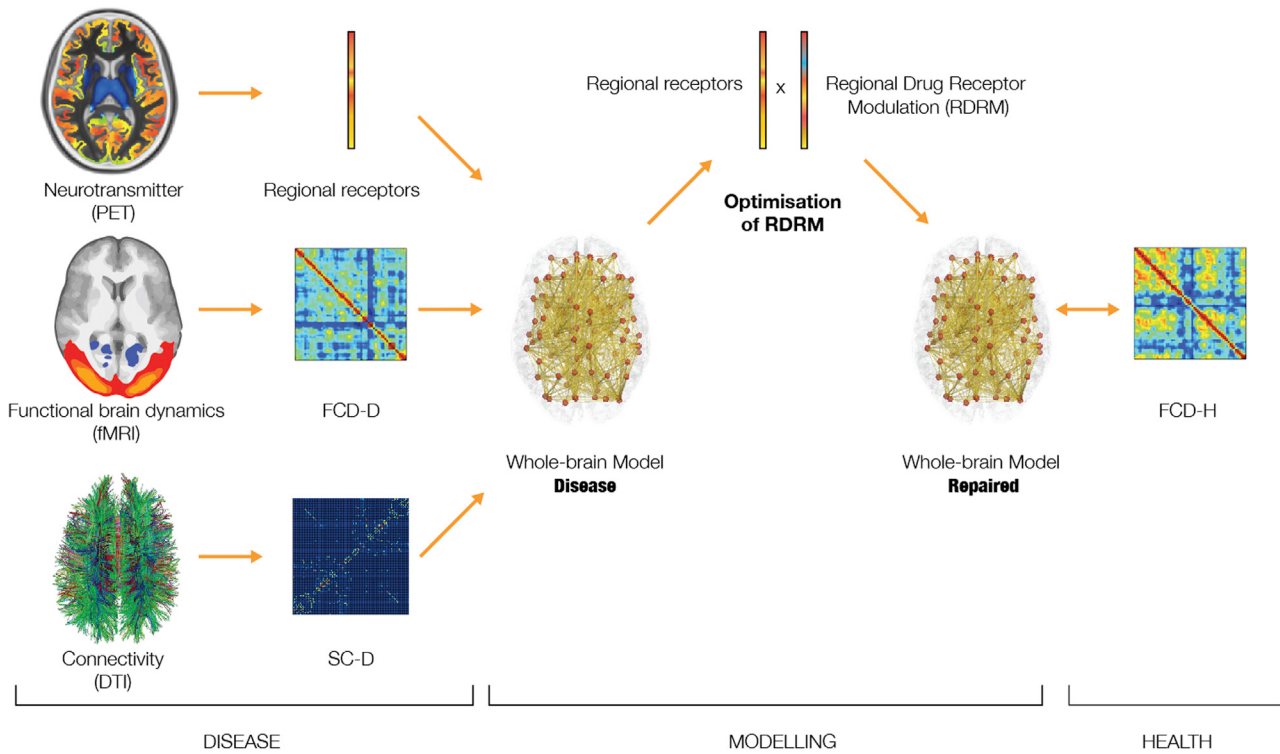


Figure 4. Potential of Using Whole-Brain Modeling for Optimal Drug Modulation Discovery

The principles of combining whole-brain computational modeling with neurotransmitter density maps to fit functional brain dynamics open up for novel rational drug discovery design. The figure provides a pipeline for how to combine structural, functional, and neurotransmitter neuroimaging data to model the disease state (leftmost). Once the model is established, the regional drug receptor modulation (RDRM) can be optimized by finding the optimal weighting of the receptor density such that the optimized model generates the functional dynamics of the healthy state.

neurotransmitter receptor density. These novel insights are only possible when using a whole-brain model given the fact that it is not possible to scramble the neurotransmitter receptor density *in vivo*. With time, this new approach could eventually lead to fundamental insights into human brain function in health and disease and be used for drug discovery and design in neuropsychiatric disorders.

STAR★METHODS

Detailed methods are provided in the online version of this paper and include the following:

- KEY RESOURCES TABLE
- CONTACT FOR REAGENT AND RESOURCE SHARING
- EXPERIMENTAL MODEL AND SUBJECT DETAILS
 - Anatomical connectivity dataset using diffusion magnetic resonance imaging
 - Functional dataset using functional magnetic resonance imaging
 - Neurotransmitter dataset using positron emission tomography
- METHOD DETAILS
 - 1. Structural connectivity
 - 2. Functional connectivity
 - 3. Neurotransmitter density

● QUANTIFICATION AND STATISTICAL ANALYSIS

- 1. Structural connectivity
- 2. Functional connectivity
- 3. Parcellation
- 4. Whole-Brain Dynamic Mean Field Model
- 5. Serotonergic Modulation

● DATA AND SOFTWARE AVAILABILITY

SUPPLEMENTAL INFORMATION

Supplemental Information includes one figure and can be found with this article online at <https://doi.org/10.1016/j.cub.2018.07.083>.

ACKNOWLEDGMENTS

G.D. is supported by the ERC Advanced Grant DYSTRUCTURE (295129), the Spanish Research Project PSI2016-75688-P, and the European Union's Horizon 2020 Framework Programme for Research and Innovation under the Specific Grant Agreement No. 785907 (Human Brain Project SGA2). M.L.K. is supported by the ERC Consolidator Grant: CAREGIVING (615539) and Center for Music in the Brain, funded by the Danish National Research Foundation (DNRF117). R.L.C.-H. is supported by the Alex Mosley Charitable Trust, and the study that yielded the empirical LSD data was carried out as part of a Beckley-Imperial research collaboration. J. Cabral is supported under the project NORTE-01-0145-FEDER-000023 from the Northern Portugal Regional Operational Program (NORTE 2020) under the Portugal 2020 Partnership Agreement through the European Regional Development Fund (FEDER).

G.M.K. and the Cimbi database were supported by a centre grant from the Lundbeck Foundation (2010-5364).

AUTHOR CONTRIBUTIONS

G.D. and M.L.K. designed and conducted the whole-brain models, with further analysis by J. Cabral and J. Cruzat. R.L.C.-H. and G.M.K. provided the experimental data. G.D., M.L.K., N.K.L., J. Cabral, J. Cruzat, P.C.W., G.M.K., and R.L.C.-H. wrote the paper.

DECLARATION OF INTERESTS

The authors declare to have no conflict of interest.

Received: May 9, 2018

Revised: June 21, 2018

Accepted: July 31, 2018

Published: September 27, 2018

REFERENCES

1. Breakspear, M. (2017). Dynamic models of large-scale brain activity. *Nat. Neurosci.* **20**, 340–352.
2. Deco, G., Jirsa, V., McIntosh, A.R., Sporns, O., and Kötter, R. (2009). Key role of coupling, delay, and noise in resting brain fluctuations. *Proc. Natl. Acad. Sci. USA* **106**, 10302–10307.
3. Deco, G., Tononi, G., Boly, M., and Kringelbach, M.L. (2015). Rethinking segregation and integration: contributions of whole-brain modelling. *Nat. Rev. Neurosci.* **16**, 430–439.
4. Deco, G., and Kringelbach, M.L. (2014). Great expectations: using whole-brain computational connectomics for understanding neuropsychiatric disorders. *Neuron* **84**, 892–905.
5. Cabral, J., Kringelbach, M.L., and Deco, G. (2017). Functional connectivity dynamically evolves on multiple time-scales over a static structural connectome: Models and mechanisms. *Neuroimage* **160**, 84–96.
6. Honey, C.J., Kötter, R., Breakspear, M., and Sporns, O. (2007). Network structure of cerebral cortex shapes functional connectivity on multiple time scales. *Proc. Natl. Acad. Sci. USA* **104**, 10240–10245.
7. Ghosh, A., Rho, Y., McIntosh, A.R., Kötter, R., and Jirsa, V.K. (2008). Noise during rest enables the exploration of the brain's dynamic repertoire. *PLoS Comput. Biol.* **4**, e1000196.
8. Biswal, B., Yetkin, F., Haughton, V., and Hyde, J. (1995). Functional connectivity in the motor cortex of resting human brain using echo-planar MRI. *Magn Reson Med.* **34**, 537–541.
9. Raichle, M.E., MacLeod, A.M., Snyder, A.Z., Powers, W.J., Gusnard, D.A., and Shulman, G.L. (2001). A default mode of brain function. *Proc. Natl. Acad. Sci. USA* **98**, 676–682.
10. Damoiseaux, J.S., Rombouts, S.A., Barkhof, F., Scheltens, P., Stam, C.J., Smith, S.M., and Beckmann, C.F. (2006). Consistent resting-state networks across healthy subjects. *Proc. Natl. Acad. Sci. USA* **103**, 13848–13853.
11. Deco, G., Cabral, J., Woolrich, M.W., Stevner, A.B.A., van Hartevelt, T.J., and Kringelbach, M.L. (2017). Single or multiple frequency generators in on-going brain activity: A mechanistic whole-brain model of empirical MEG data. *Neuroimage* **152**, 538–550.
12. Cabral, J., Luckhoo, H., Woolrich, M., Joensson, M., Mohseni, H., Baker, A., Kringelbach, M.L., and Deco, G. (2014). Exploring mechanisms of spontaneous functional connectivity in MEG: how delayed network interactions lead to structured amplitude envelopes of band-pass filtered oscillations. *Neuroimage* **90**, 423–435.
13. Ghosh, A., Rho, Y., McIntosh, A.R., Kötter, R., and Jirsa, V.K. (2008). Cortical network dynamics with time delays reveals functional connectivity in the resting brain. *Cogn Neurodyn* **2**, 115–120.
14. Kringelbach, M.L., McIntosh, A.R., Ritter, P., Jirsa, V.K., and Deco, G. (2015). The rediscovery of slowness: exploring the timing of cognition. *Trends Cogn. Sci.* **19**, 616–628.
15. Bargmann, C.I. (2012). Beyond the connectome: how neuromodulators shape neural circuits. *BioEssays* **34**, 458–465.
16. Smythies, J. (2005). Section V. Serotonin system. *Int. Rev. Neurobiol.* **64**, 217–268.
17. Marder, E. (2012). Neuromodulation of neuronal circuits: back to the future. *Neuron* **76**, 1–11.
18. Beliveau, V., Ganz, M., Feng, L., Ozanne, B., Højgaard, L., Fisher, P.M., Svarer, C., Greve, D.N., and Knudsen, G.M. (2017). A High-Resolution In Vivo Atlas of the Human Brain's Serotonin System. *J. Neurosci.* **37**, 120–128.
19. Tzourio-Mazoyer, N., Landau, B., Papathanassiou, D., Crivello, F., Etard, O., Delcroix, N., Mazoyer, B., and Joliot, M. (2002). Automated anatomical labeling of activations in SPM using a macroscopic anatomical parcellation of the MNI MRI single-subject brain. *Neuroimage* **15**, 273–289.
20. Carhart-Harris, R.L., Muthukumaraswamy, S., Roseman, L., Kaelen, M., Droog, W., Murphy, K., Tagliazucchi, E., Schenberg, E.E., Nest, T., Orban, C., et al. (2016). Neural correlates of the LSD experience revealed by multimodal neuroimaging. *Proc. Natl. Acad. Sci. USA* **113**, 4853–4858.
21. Kaelen, M., Barrett, F.S., Roseman, L., Lorenz, R., Family, N., Bolstridge, M., Curran, H.V., Feilding, A., Nutt, D.J., and Carhart-Harris, R.L. (2015). LSD enhances the emotional response to music. *Psychopharmacology (Berl.)* **232**, 3607–3614.
22. Nichols, D.E. (2016). Psychedelics. *Pharmacol. Rev.* **68**, 264–355.
23. Hagmann, P., Cammoun, L., Gigandet, X., Meuli, R., Honey, C.J., Wedeen, V.J., and Sporns, O. (2008). Mapping the structural core of human cerebral cortex. *PLoS Biol.* **6**, e159.
24. Cabral, J., Kringelbach, M.L., and Deco, G. (2014). Exploring the network dynamics underlying brain activity during rest. *Prog. Neurobiol.* **114**, 102–131.
25. Deco, G., Ponce-Alvarez, A., Hagmann, P., Romani, G.L., Mantini, D., and Corbetta, M. (2014). How local excitation-inhibition ratio impacts the whole brain dynamics. *J. Neurosci.* **34**, 7886–7898.
26. Brunel, N., and Wang, X.J. (2001). Effects of neuromodulation in a cortical network model of object working memory dominated by recurrent inhibition. *J. Comput. Neurosci.* **11**, 63–85.
27. Hansen, E.C., Battaglia, D., Spiegler, A., Deco, G., and Jirsa, V.K. (2015). Functional connectivity dynamics: modeling the switching behavior of the resting state. *Neuroimage* **105**, 525–535.
28. Allen, E.A., Damaraju, E., Plis, S.M., Erhardt, E.B., Eichele, T., and Calhoun, V.D. (2014). Tracking whole-brain connectivity dynamics in the resting state. *Cereb. Cortex* **24**, 663–676.
29. Deco, G., and Kringelbach, M.L. (2016). Metastability and Coherence: Extending the Communication through Coherence Hypothesis Using A Whole-Brain Computational Perspective. *Trends Neurosci.* **39**, 125–135.
30. Messé, A., Rudrauf, D., Benali, H., and Marrelec, G. (2014). Relating structure and function in the human brain: relative contributions of anatomy, stationary dynamics, and non-stationarities. *PLoS Comput. Biol.* **10**, e1003530.
31. Deco, G., Kringelbach, M.L., Jirsa, V.K., and Ritter, P. (2017). The dynamics of resting fluctuations in the brain: metastability and its dynamical cortical core. *Sci. Rep.* **7**, 3095.
32. Halberstadt, A.L. (2015). Recent advances in the neuropsychopharmacology of serotonergic hallucinogens. *Behav. Brain Res.* **277**, 99–120.
33. King, M.V., Marsden, C.A., and Fone, K.C. (2008). A role for the 5-HT(1A), 5-HT4 and 5-HT6 receptors in learning and memory. *Trends Pharmacol. Sci.* **29**, 482–492.
34. Švob Štrac, D., Pivac, N., and Mück-Seler, D. (2016). The serotonergic system and cognitive function. *Transl. Neurosci.* **7**, 35–49.

35. Atasoy, S., Deco, G., Kringelbach, M.L., and Pearson, J. (2018). Harmonic brain modes: a unifying framework for linking space and time in brain dynamics. *Neuroscientist* 24, 277–293.
36. Carhart-Harris, R.L., and Nutt, D.J. (2017). Serotonin and brain function: a tale of two receptors. *J. Psychopharmacol. (Oxford)* 31, 1091–1120.
37. Azmitia, E.C., and Gannon, P.J. (1986). The primate serotonergic system: a review of human and animal studies and a report on *Macaca fascicularis*. *Adv. Neurol.* 43, 407–468.
38. Wilson, M.A., and Molliver, M.E. (1991). The organization of serotonergic projections to cerebral cortex in primates: retrograde transport studies. *Neuroscience* 44, 555–570.
39. Jacobs, B.L., and Azmitia, E.C. (1992). Structure and function of the brain serotonin system. *Physiol. Rev.* 72, 165–229.
40. Serretti, A., Calati, R., Mandelli, L., and De Ronchi, D. (2006). Serotonin transporter gene variants and behavior: a comprehensive review. *Curr. Drug Targets* 7, 1659–1669.
41. Amara, S.G., and Kuhar, M.J. (1993). Neurotransmitter transporters: recent progress. *Annu. Rev. Neurosci.* 16, 73–93.
42. Preller, K.H., Herdener, M., Pokorny, T., Planzer, A., Krahenmann, R., Stämpfli, P., Liechti, M.E., Seifritz, E., and Vollenweider, F.X. (2017). The Fabric of Meaning and Subjective Effects in LSD-Induced States Depend on Serotonin 2A Receptor Activation. *Curr. Biol.* 27, 451–457.
43. Carhart-Harris, R.L., Kaelen, M., Bolstridge, M., Williams, T.M., Williams, L.T., Underwood, R., Feilding, A., and Nutt, D.J. (2016). The paradoxical psychological effects of lysergic acid diethylamide (LSD). *Psychol. Med.* 46, 1379–1390.
44. Nichols, D.E. (2018). Chemistry and Structure-Activity Relationships of Psychedelics. *Curr. Top. Behav. Neurosci.* 36, 1–43.
45. Shine, J.M., Auburn, M.J., Breakspear, M., and Poldrack, R.A. (2018). The modulation of neural gain facilitates a transition between functional segregation and integration in the brain. *eLife* 7, e31130.
46. Atasoy, S., Roseman, L., Kaelen, M., Kringelbach, M.L., Deco, G., and Carhart-Harris, R. (2017). Connectome-harmonic decomposition of human brain activity reveals dynamical repertoire re-organization under LSD. *Sci. Rep.* 7, 17661.
47. Kirsch, I., Deacon, B.J., Huedo-Medina, T.B., Scoboria, A., Moore, T.J., and Johnson, B.T. (2008). Initial severity and antidepressant benefits: a meta-analysis of data submitted to the Food and Drug Administration. *PLoS Med.* 5, e45.
48. Fountoulakis, K.N., and Moller, H.J. (2011). Efficacy of antidepressants: are-analysis and re-interpretation of the Kirsch data. *Int. J. Neuropsychopharmacol.* 14, 405–412.
49. Holtzheimer, P.E., and Mayberg, H.S. (2011). Stuck in a rut: rethinking depression and its treatment. *Trends Neurosci.* 34, 1–9.
50. Kapur, S., Phillips, A.G., and Insel, T.R. (2012). Why has it taken so long for biological psychiatry to develop clinical tests and what to do about it? *Mol. Psychiatry* 17, 1174–1179.
51. Conn, P.J., Tamminga, C., Schoepp, D.D., and Lindsley, C. (2008). Schizophrenia: moving beyond monoamine antagonists. *Mol. Interv.* 8, 99–107.
52. Starcevic, V., and Brakoulias, V. (2008). Symptom subtypes of obsessive-compulsive disorder: are they relevant for treatment? *Aust. N. Z. J. Psychiatry* 42, 651–661.
53. Trusheim, M.R., Berndt, E.R., and Douglas, F.L. (2007). Stratified medicine: strategic and economic implications of combining drugs and clinical biomarkers. *Nat. Rev. Drug Discov.* 6, 287–293.
54. Cuthbert, B.N., and Insel, T.R. (2013). Toward the future of psychiatric diagnosis: the seven pillars of RDoC. *BMC Med.* 11, 126.
55. Stephan, K.E., Bach, D.R., Fletcher, P.C., Flint, J., Frank, M.J., Friston, K.J., Heinz, A., Huys, Q.J.M., Owen, M.J., Binder, E.B., et al. (2016). Charting the landscape of priority problems in psychiatry, part 1: classification and diagnosis. *Lancet Psychiatry* 3, 77–83.
56. Stephan, K.E., Binder, E.B., Breakspear, M., Dayan, P., Johnstone, E.C., Meyer-Lindenberg, A., Schnyder, U., Wang, X.J., Bach, D.R., Fletcher, P.C., et al. (2016). Charting the landscape of priority problems in psychiatry, part 2: pathogenesis and aetiology. *Lancet Psychiatry* 3, 84–90.
57. Berridge, K.C., and Kringelbach, M.L. (2015). Pleasure systems in the brain. *Neuron* 86, 646–664.
58. Rømer Thomsen, K., Whybrow, P.C., and Kringelbach, M.L. (2015). Reconceptualizing anhedonia: novel perspectives on balancing the pleasure networks in the human brain. *Front. Behav. Neurosci.* 9, 49.
59. Carhart-Harris, R.L., Roseman, L., Haijen, E., Erritzoe, D., Watts, R., Branchi, I., and Kaelen, M. (2018). Psychedelics and the essential importance of context. *J. Psychopharmacol. (Oxford)* 32, 725–731.
60. Knudsen, G.M., Jensen, P.S., Erritzoe, D., Baaré, W.F., Ettrup, A., Fisher, P.M., Gillings, N., Hansen, H.D., Hansen, L.K., Hasselbalch, S.G., et al. (2016). The center for integrated molecular brain imaging (Cimbi) database. *Neuroimage* 124 (Pt B), 1213–1219.
61. Kaelen, M., Lorenz, R., Barrett, F.S., Roseman, L., Orban, C., Santos-Ribeiro, A., Wall, M.B., Feilding, A., Nutt, D., Muthukumaraswamy, S., et al. (2017). Effects of LSD on music-evoked brain activity. *bioRxiv*. <https://doi.org/10.1101/153031>.
62. Olesen, O.V., Sibomana, M., Keller, S.H., Andersen, F., Jensen, J., Holm, S., Svarer, C., and Hojgaard, L. (2009). Spatial resolution of the HRRT PET scanner using 3D-OSEM PSF reconstruction. In *Proceedings from the 2009 IEEE Nuclear Science Symposium Conference Record (IEEE)*, pp. 3789–3790.
63. Ettrup, A., da Cunha-Bang, S., McMahon, B., Lehel, S., Dyssegård, A., Skibsted, A.W., Jørgensen, L.M., Hansen, M., Baandrup, A.O., Bache, S., et al. (2014). Serotonin 2A receptor agonist binding in the human brain with [¹¹C]Cimbi-36. *J. Cereb. Blood Flow Metab.* 34, 1188–1196.
64. Ettrup, A., Svarer, C., McMahon, B., da Cunha-Bang, S., Lehel, S., Møller, K., Dyssegård, A., Ganz, M., Beliveau, V., Jørgensen, L.M., et al. (2016). Serotonin 2A receptor agonist binding in the human brain with [¹¹C]Cimbi-36: Test-retest reproducibility and head-to-head comparison with the antagonist [¹⁸F]altanserin. *Neuroimage* 130, 167–174.
65. Comtat, C., Sureau, F., Sibomana, M., Hong, I., Sjoholm, N., and Trebossen, R. (2008). Image based resolution modeling for the HRRT OSEM reconstructions software. In *Proceedings of the 2008 IEEE Nuclear Science Symposium Conference Record (IEEE)*, pp. 4120–4123.
66. Sureau, F.C., Reader, A.J., Comtat, C., Leroy, C., Ribeiro, M.-J., Buvat, I., and Trébossen, R. (2008). Impact of image-space resolution modeling for studies with the high-resolution research tomograph. *J. Nucl. Med.* 49, 1000–1008.
67. Woods, R.P., Cherry, S.R., and Mazziotta, J.C. (1992). Rapid automated algorithm for aligning and reslicing PET images. *J. Comput. Assist. Tomogr.* 16, 620–633.
68. Jovicich, J., Czanner, S., Greve, D., Haley, E., van der Kouwe, A., Gollub, R., Kennedy, D., Schmitt, F., Brown, G., Macfall, J., et al. (2006). Reliability in multi-site structural MRI studies: effects of gradient non-linearity correction on phantom and human data. *Neuroimage* 30, 436–443.
69. Fischl, B. (2012). FreeSurfer. *Neuroimage* 62, 774–781.
70. Greve, D.N., and Fischl, B. (2009). Accurate and robust brain image alignment using boundary-based registration. *Neuroimage* 48, 63–72.
71. Postelnicu, G., Zollei, L., and Fischl, B. (2009). Combined volumetric and surface registration. *IEEE Trans. Med. Imaging* 28, 508–522.
72. Jenkinson, M., Bannister, P., Brady, M., and Smith, S. (2002). Improved optimization for the robust and accurate linear registration and motion correction of brain images. *Neuroimage* 17, 825–841.
73. Collins, D.L., Neelin, P., Peters, T.M., and Evans, A.C. (1994). Automatic 3D intersubject registration of MR volumetric data in standardized Talairach space. *J. Comput. Assist. Tomogr.* 18, 192–205.
74. Gordon, E.M., Laumann, T.O., Adeyemo, B., Huckins, J.F., Kelley, W.M., and Petersen, S.E. (2016). Generation and Evaluation of a Cortical Area Parcellation from Resting-State Correlations. *Cereb. Cortex* 26, 288–303.

75. Eickhoff, S.B., Constable, R.T., and Yeo, B.T.T. (2018). Topographic organization of the cerebral cortex and brain cartography. *Neuroimage* 170, 332–347.
76. Behrens, T.E., Woolrich, M.W., Jenkinson, M., Johansen-Berg, H., Nunes, R.G., Clare, S., Matthews, P.M., Brady, J.M., and Smith, S.M. (2003). Characterization and propagation of uncertainty in diffusion-weighted MR imaging. *Mag Reson Med.* 50, 1077–1088.
77. Behrens, T.E., Berg, H.J., Jbabdi, S., Rushworth, M.F., and Woolrich, M.W. (2007). Probabilistic diffusion tractography with multiple fibre orientations: What can we gain? *Neuroimage* 34, 144–155.
78. Beckmann, C.F., and Smith, S.M. (2004). Probabilistic independent component analysis for functional magnetic resonance imaging. *IEEE Trans. Med. Imaging* 23, 137–152.
79. Wong, K.F., and Wang, X.J. (2006). A recurrent network mechanism of time integration in perceptual decisions. *J. Neurosci.* 26, 1314–1328.
80. Abbott, L.F., and Chance, F.S. (2005). Drivers and modulators from push-pull and balanced synaptic input. *Prog. Brain Res.* 149, 147–155.
81. Burns, B.D., and Webb, A. (1976). The spontaneous activity of neurones in the cat's cerebral cortex. *Proc R Soc Lond B Biol Sci.* 194, 211–223.
82. Koch, K.W., and Fuster, J.M. (1989). Unit activity in monkey parietal cortex related to haptic perception and temporary memory. *Exp. Brain Res.* 76, 292–306.
83. Softky, W.R., and Koch, C. (1993). The highly irregular firing of cortical cells is inconsistent with temporal integration of random EPSPs. *J. Neurosci.* 13, 334–350.
84. Shadlen, M.N., and Newsome, W.T. (1998). The variable discharge of cortical neurons: implications for connectivity, computation, and information coding. *J. Neurosci.* 18, 3870–3896.
85. Stephan, K.E., Weiskopf, N., Drysdale, P.M., Robinson, P.A., and Friston, K.J. (2007). Comparing hemodynamic models with DCM. *Neuroimage* 38, 387–401.
86. Glerean, E., Salmi, J., Lahnakoski, J.M., Jääskeläinen, I.P., and Sams, M. (2012). Functional magnetic resonance imaging phase synchronization as a measure of dynamic functional connectivity. *Brain Connect.* 2, 91–101.
87. Buckner, R.L., Sepulcre, J., Talukdar, T., Krienen, F.M., Liu, H., Hedden, T., Andrews-Hanna, J.R., Sperling, R.A., and Johnson, K.A. (2009). Cortical hubs revealed by intrinsic functional connectivity: mapping, assessment of stability, and relation to Alzheimer's disease. *J. Neurosci.* 29, 1860–1873.
88. Achard, S., Salvador, R., Whitcher, B., Suckling, J., and Bullmore, E. (2006). A resilient, low-frequency, small-world human brain functional network with highly connected association cortical hubs. *J. Neurosci.* 26, 63–72.
89. Grasso, C., Li Volsi, G., and Barresi, M. (2016). Serotonin modifies the spontaneous spiking activity of gracile nucleus neurons in rats: role of 5-HT1A and 5-HT2 receptors. *Arch. Ital. Biol.* 154, 39–49.
90. Licata, F., Li Volsi, G., Maugeri, G., and Santangelo, F. (1993). Excitatory and inhibitory effects of 5-hydroxytryptamine on the firing rate of medial vestibular nucleus neurons in the rat. *Neurosci. Lett.* 154, 195–198.
91. Licata, F., Li Volsi, G., Maugeri, G., and Santangelo, F. (1995). Neuronal responses to 5-hydroxytryptamine in the red nucleus of rats. *Exp. Brain Res.* 107, 215–220.
92. Licata, F., Li Volsi, G., Maugeri, G., Ciranna, L., and Santangelo, F. (1993). Serotonin-evoked modifications of the neuronal firing rate in the superior vestibular nucleus: a microiontophoretic study in the rat. *Neuroscience* 52, 941–949.
93. Schmied, A., Farin, D., Amalric, M., and Dormont, J.F. (1991). Changes in motor performance and rubral single unit activity in cats after microinjections of serotonin into the red nucleus area. *Brain Res.* 567, 91–100.
94. Chance, F.S., Abbott, L.F., and Reyes, A.D. (2002). Gain modulation from background synaptic input. *Neuron* 35, 773–782.

STAR★METHODS

KEY RESOURCES TABLE

REAGENT or RESOURCE	SOURCE	IDENTIFIER
Software and Algorithms		
Whole-brain modeling	Custom software	https://github.com/decolab/cb-neuromod
MATLAB 2014b	MathWorks	https://www.mathworks.com
SPM	Wellcome Department of Cognitive Neurology, London, UK	https://www.fil.ion.ucl.ac.uk/spm/
FSL	FMRIB Software Library	https://fsl.fmrib.ox.ac.uk/fsl/fslwiki/

CONTACT FOR REAGENT AND RESOURCE SHARING

Further information and requests for resources should be directed to and will be fulfilled by the Lead Contact: Morten L. Kringelbach (morten.kringelbach@psych.ox.ac.uk).

EXPERIMENTAL MODEL AND SUBJECT DETAILS

Three empirical datasets using human participants were used:

Anatomical connectivity dataset using diffusion magnetic resonance imaging

We used diffusion MRI (dMRI) data collected in 16 healthy right-handed participants at Aarhus University, Denmark (5 women, mean age: 24.8 ± 2.5). The study was approved by the internal research board at CFIN, Aarhus University, Denmark. Ethics approval was granted by the Research Ethics Committee of the Central Denmark Region (De Videnskabsetiske Komitéer for Region Midtjylland). Written informed consent was obtained from all participants prior to participation.

Functional dataset using functional magnetic resonance imaging

All 15 participants (four women; mean age, 30.5 ± 8.0) were recruited via word of mouth and provided written informed consent to participate after study briefing and screening for physical and mental health. The study was approved by the National Research Ethics Service committee London-West London and was conducted in accordance with the revised declaration of Helsinki (2000), the International Committee on Harmonization of Good Clinical Practice guidelines, and National Health Service Research Governance Framework. Imperial College London sponsored the research, which was conducted under a Home Office license for research with schedule 1 drugs. The screening for physical health included electrocardiogram (ECG), routine blood tests, and urine test for recent drug use and pregnancy. A psychiatric interview was conducted and participants provided full disclosure of their drug use history. Key exclusion criteria included: < 21 years of age, personal history of diagnosed psychiatric illness, immediate family history of a psychotic disorder, an absence of previous experience with a classic psychedelic drug (e.g., LSD, mescaline, psilocybin/magic mushrooms or DMT/Ayahuasca), any psychedelic drug use within 6 weeks of the first scanning day, pregnancy, problematic alcohol use (i.e., > 40 units consumed per week), or a medically significant condition rendering the volunteer unsuitable for the study.

Neurotransmitter dataset using positron emission tomography

The participants were healthy male and female controls from the Cimbi database [60]; all data from this database are freely accessible. The data analysis was restricted to include individuals aged between 18 and 45 years. Participants were recruited by advertisement for different research protocols approved by the Ethics Committee of Copenhagen and Frederiksberg, Denmark. A total of 232 positron emission tomography (PET) scans and corresponding structural MRI scans were acquired for 210 individual participants; 189 participants had only one scan, 20 participants had two scans, and a single had three scans.

METHOD DETAILS

Here we describe the methods for obtaining 1) *structural connectivity*: probabilistic tractography derived from the dMRI, 2) *functional connectivity*: functional dynamics estimated from the fMRI in the placebo and LSD condition, and 3) *neurotransmitter density*: estimation of the density of the 5HT-2A receptors that has been obtained using PET.

1. Structural connectivity

Participants and acquisition

We used dMRI data collected in 16 healthy right-handed participants at Aarhus University, Denmark (5 women, mean age: 24.8 ± 2.5). The imaging data were recorded in a single session on a 3 T Siemens Skyra scanner at CFIN, Aarhus University, Denmark. The following parameters were used for the structural MRI T1 scan: voxel size of 1 mm^3 ; reconstructed matrix size 256×256 ; echo time (TE) of 3.8 ms and repetition time (TR) of 2300 ms. dMRI data were collected using TR = 9000 ms, TE = 84 ms, flip angle = 90° , reconstructed matrix size of 106×106 , voxel size of $1.98 \times 1.98\text{ mm}$ with slice thickness of 2 mm and a bandwidth of 1745 Hz/Px. Furthermore, the data were recorded with 62 optimal nonlinear diffusion gradient directions at $b = 1500\text{ s/mm}^2$. One non-diffusion weighted image ($b = 0$) per 10 diffusion-weighted images was acquired, approximately. One of dMRI images was collected applying anterior to posterior phase encoding direction and the other acquired in the opposite direction.

2. Functional connectivity

The functional data is described in details in a previous study [20] but here we briefly summarize the study setting and acquisition protocol.

Study setting and overview

Screening took place at Imperial's clinical research facility (ICRF) at the Hammersmith hospital campus. Participants who were found eligible for the study attended two study days that were separated by at least 14 days. On one day, the participants received placebo, and on the other day they received LSD. The order of the conditions was balanced across participants, and participants were blind to this order but the researchers were not.

On scanning days, volunteers arrived at the study center at 8:00am. They were briefed in detail about the study day schedule, gave a urine test for recent drug use and pregnancy, and carried out a breathalyser test for recent alcohol use. A cannula was inserted into a vein in the antecubital fossa by a medical doctor and secured. The participants were encouraged to close their eyes and relax in a reclined position when the drug was administered. All participants received 75 μg of LSD, administered intravenously via a 10ml solution infused over a two minutes' period, followed by an infusion of saline. The administration was followed by an acclimatization period of approximately 60 min, in which (for at least some of the time) participants were encouraged to relax and lie with their eyes closed inside a mock MRI scanner. This functioned to psychologically prepare the participants for being in the subsequent (potentially anxiogenic) MRI scanning environment.

Participants reported noticing subjective drug effects between 5 to 15 min post-dosing, and these approached peak intensity between 60 to 90 min post-dosing. The duration of a subsequent plateau of drug effects varied among individuals but was generally maintained for approximately four hours post-dosing. MRI scanning started approximately 70 min post-dosing, and lasted for approximately 60 min. This included a structural scan and BOLD fMRI. Once the subjective effects of LSD had sufficiently subsided, the study psychiatrist assessed the participant's suitability for discharge.

Scanning design and content

The BOLD scanning consisted of three eyes-closed resting state scans, each lasting seven minutes. After each seven-minute scan, VAS ratings were performed in the scanner via a response-box. The first and third scans were eyes-closed rest but the second scan also incorporated listening to two excerpts of music from two songs by ambient artist Robert Rich [61]. The stimuli were both 7.3 min long and were balanced in their acoustic properties, and rich in timbre, but not in rhythm. Pre-study assessments in a separate group confirmed balance for their emotional potency. In order to reduce interference of fMRI scanning noise with the music experience, volume-maximization and broadband compression was carried out using Ableton Live 9 software. Each participant listened to both stimuli, in a balanced order across conditions. Prior to each scan, participants were instructed via onscreen instructions to close their eyes and relax. Here we used the music + LSD condition since this has been demonstrated to yield a larger effect on brain activity [20] but we also found the effects for LSD without music.

Anatomical Scans

Imaging was performed on a 3T GE HDx system. These were 3D fast spoiled gradient echo scans in an axial orientation, with field of view = $256 \times 256 \times 192$ and matrix = $256 \times 256 \times 192$ to yield 1mm isotropic voxel resolution. TR/TE = 7.9/3.0ms; inversion time = 450ms; flip angle = 20° .

BOLD fMRI Data Acquisition

Two BOLD-weighted fMRI data were acquired using a gradient echo planer imaging sequence, TR/TE = 2000/35ms, field-of-view = 220mm, 64×64 acquisition matrix, parallel acceleration factor = 2, 90° flip angle. Thirty-five oblique axial slices were acquired in an interleaved fashion, each 3.4mm thick with zero slice gap (3.4mm isotropic voxels). The precise length of each of the two BOLD scans was 7:20 min.

3. Neurotransmitter density

The methods used to obtain the 5HT2A receptor density distribution is described in details elsewhere [18] but in the following we briefly summarize the main methods.

PET and structural MRI

PET data were acquired in list mode on a Siemens HRRT scanner operating in 3D acquisition mode with an approximate in-plane resolution of 2 mm (1.4 mm in the center of the field of view and 2.4 mm in cortex[62]). The PET scanning used the recently developed [¹¹C]Cimbi-36 as a selective serotonin 2A (5-HT2A) receptor agonist radioligand [63, 64]. The radioligands for the other serotonin

receptors are described in the paper by Beliveau and colleagues [18]. PET frames were reconstructed using a 3D-OSEM-PSF algorithm [65, 66]. Scan time and frame length were designed according to the radiotracer characteristics. Dynamic PET frames were realigned using AIR 5.2.5[67]. T1- and T2-weighted structural MRI were acquired on four different Siemens scanners with standard parameters. All structural MRIs (T1 and T2) were unwarped offline using FreeSurfer's gradient_-nonlin_unwarp version 0.8 or online on the scanner [68]. For further details on structural MRI acquisition parameters, see [60].

Further processing was performed with FreeSurfer 5.3 [69] (<http://surfer.nmr.mgh.harvard.edu>) using a surface and a volume stream. The individual cortical surfaces were reconstructed using the structural MRI corrected for gradient nonlinearities. The pial surfaces were further refined using T2-weighted structural images and corrected manually where necessary. PET-MR coregistration was estimated using boundary-based registration[70] between the time- weighted sum of the PET time–activity curves (TACs) and the structural MRI. Additionally, the transformation from individual MR space to normal MNI152 space was estimated with combined volume–surface (CVS) registration [71].

QUANTIFICATION AND STATISTICAL ANALYSIS

First we provide a general overview of the analysis pipeline used to integrate structural and functional connectivity (diffusion magnetic resonance imaging, dMRI, and functional magnetic resonance, fMRI) with neurotransmission (positron emission tomography, PET) in a model of the placebo and LSD response in healthy participants (see [Figure 1](#) in main paper).

This overview is subsequently followed by the specific methods, namely:

1. Structural connectivity: probabilistic tractography derived from the dMRI
2. Functional connectivity: functional dynamics estimated from the fMRI in the placebo and LSD condition
3. Parcellation: all structural, functional and neuromodulation data are integrated into the Automated Anatomical Labeling (AAL) parcellation
4. Whole-brain computational model: a dynamic mean field model was used to integrate the available data to fit the placebo condition
5. Neuromodulation in whole-brain model: integration of the neurotransmission data by changing the gain of neurons in the placebo-fitted whole-brain model in order to fit the LSD condition

1. Structural connectivity

Tractography

For the present study, we used the structural connectivity between the 90 AAL regions obtained in a previous study [11] averaged across 16 healthy young adults (5 females, mean \pm SD age: 24.75 ± 2.54). The linear registration tool from the FSL toolbox (www.fmrib.ox.ac.uk/fsl, FMRIB, Oxford)[72] was used to coregister the EPI image to the T1-weighted structural image. The T1-weighted image was co-registered to the T1 template of ICBM152 in MNI space[73]. The resulting transformations were concatenated and inverted and further applied to warp the AAL template [19] from MNI space to the EPI native space, where interpolation using nearest-neighbor method ensured that the discrete labeling values were preserved. Thus the brain parcellations were conducted in each individual's native space. We generated the structural connectivity (SC) maps for each participant using the dMRI data acquired. We processed the two datasets acquired (each with different phase encoding to optimize signal in difficult regions). The construction of these structural connectivity maps or structural brain networks consisted of a three-step process. First, the regions of the whole-brain network were defined using the AAL template as used in the functional MRI data. Second, the connections between nodes in the whole-brain network (i.e., edges) were estimated using probabilistic tractography. Third, data was averaged across participants.

We note that the recent results from Gordon and colleagues would seem to suggest that the AAL parcellation is less than optimal, in that the AAL was the least homogeneous parcellation scheme tested [74]. Nevertheless, it is not clear if the methodology used in that paper is particularly meaningful. Indeed, in the recent paper by Eickhoff and colleagues, they review the literature on the topographic organization of the brain and conclude that it is presently not clear what is the right spatial parcellation [75]. Both papers are mostly concerned with the spatial organization of the brain, while in this ms, we focus on the spatiotemporal global dynamics. For this goal, AAL would appear to be a good choice for the following reasons: 1) AAL yields excellent significant results in the whole-brain literature in general [5, 12, 31]. 2) The relative low number of parcels in the AAL is highly suitable for our very extensive computational demands.

We used the FSL diffusion toolbox (Fdt) in FSL to carry out the various processing stages of the diffusion MRI data. We used the default parameters of this imaging pre-processing pipeline on all participants. Following this preprocessing, we estimated the local probability distribution of fiber direction at each voxel [76]. We used the probtrackx tool in Fdt to provide automatic estimation of crossing fibers within each voxel. This has been shown to significantly improve the tracking sensitivity of non-dominant fiber populations in the human brain [77].

The connectivity probability from a seed voxel i to another voxel j was defined by the proportion of fibers passing through voxel i that reach voxel j using a sampling of 5000 streamlines per voxel [77]. This was extended from the voxel level to the region level, i.e., in an AAL parcel consisting of n voxels, $5000 \times n$ fibers were sampled. The connectivity probability P_{ij} from region i to region j is calculated as the number of sampled fibers in region i that connect the two regions divided by $5000 \times n$, where n is the number of voxels in region i . We threshold the SC matrix at 0.1%, i.e., five streamlines.

For each brain region, the connectivity probability to each of the other 89 regions within the AAL was calculated. Due to the dependence of tractography on the seeding location, the probability from i to j is not necessarily equivalent to that from j to i . However, these two probabilities are highly correlated across the brain for all participants (the least Pearson $r = 0.70$, $p < 10^{-50}$). As directionality of connections cannot be determined based on diffusion MRI, the unidirectional connectivity probability P_{ij} between regions i and j was defined by averaging these two connectivity probabilities. This unidirectional connectivity was considered as a measure of the structural connectivity between the two areas, with $C_{ij} = C_{ji}$. We implemented the calculation of regional connectivity probability using in-house Perl scripts. For both phase encoding directions, 90x90 symmetric weighted networks were constructed based on the AAL90 parcellation, and normalized by the number of voxels in each AAL region; thus representing the structural connectivity network organization of the brain.

We applied the AAL90 template using the FLIRT tool from the FSL toolbox (www.fmrib.ox.ac.uk/fsl, FMRIB, Oxford) to coregister the b0 image in diffusion MRI space to the T1-weighted structural image and then to the T1 template of ICBM152 in MNI space [73]. The two transformation matrices from these coregistration steps were concatenated and inversed to subsequently be applied to warp the AAL templates [19] from MNI space to the diffusion MRI native space.

2. Functional connectivity

Preprocessing

We first preprocessed the fMRI data using MELODIC 3.14 [78], part of FSL (FMRIB's Software Library, www.fmrib.ox.ac.uk/fsl) with standard parameters and not discarding any ICA components. Head motion during the experiments was corrected using the FSL tools mcflirt as part of the standard MELODIC pipeline and was within normal acceptable range for neuroimaging experiments. Specifically, the cloud plot in Figure S7 in the original LSD data paper [20] shows that motion is similar in the placebo and LSD conditions in terms of its effects on biasing potential related motion artifacts. For each participant and for each brain state (i.e., placebo and LSD), we used FSL tools to extract and average the BOLD signals from all voxels within each ROI defined in the AAL atlas (considering only the 90 cortical and subcortical non-cerebellar brain regions) [19]. We computed both the static functional connectivity (FC) and the functional connectivity dynamics (FCD). In brief, the FCD is a matrix that expresses the spatiotemporal statistics of a snapshot of FC across different sliding windows. The matrix is thus not locked in time to a particular instance and the spatiotemporal evolution (between different sessions, subjects or simulations) is thus not aligned. As a consequence, comparing the differences between empirical and whole-brain model level of fitting, we need to compare the distributions of the elements of those matrices. For this the standard method is to use the Kolmogorov-Smirnov (KS) distance (see details in [31]) where a smaller value means better fit. For the grand average FC, the standard approach is to use correlation between the FC matrices, because the matrices are aligned and what matters are the correlations between different pairs, i.e., a higher correlation value would mean a better fit. More specifically, we computed FC and FCD in the following ways:

1) Static Functional Connectivity

The static FC is defined as the $N \times N$ matrix of BOLD signal correlations between brain areas computed over the whole recording time. The empirical and simulated FC matrices were compared by computing the Pearson correlation between their upper triangular elements (due to matrix symmetry).

2) Functional Connectivity Dynamics

To consider the temporal dynamics of resting-state FC, we computed the FC over a sliding window of 30 TR with increments of 2 TR, resulting in a time-evolving FC matrix (see Figure 2). Subsequently, we compute a time-versus-time matrix of Functional Connectivity Dynamics (FCD), where each entry, $FCD(t_x, t_y)$, corresponds to the correlation between the FC centered at times t_x and the FC centered at t_y .

Typically, the FCD matrices computed in the resting-state reveal a characteristic checkered pattern indicative of spontaneous switching between different FC patterns. Importantly, the distribution of FCD values contains valuable information regarding the time-dependencies of resting-state activity and we use it to as way to characterize the dynamical properties of resting-state activity in the different conditions and simulations. To do so, we generate the distributions of the upper triangular elements of the FCD matrices over all participants in a given condition (LSD or placebo), as well as of the FCD matrices obtained from simulations. The different distributions are then compared using the Kolmogorov-Smirnov (KS) distance, allowing for a meaningful evaluation of the model performance in predicting the changes observed in resting-state FC in dynamical terms.

3. Parcellation

Based on our previous whole-brain studies we used the AAL atlas but considering only the 90 cortical and subcortical non-cerebellar brain regions [19]. All structural, functional and neuromodulation data was integrated using this atlas. We used FSL tools on the freely available 5HT2A receptor density map in MNI space to extract the average receptor density for each individual AAL region.

4. Whole-Brain Dynamic Mean Field Model

We used a network model to simulate spontaneous brain activity at the whole-brain level, where each node represents a brain area and the links represent the white matter connections between them. The activity in each brain area is represented by the Dynamic Mean Field (DMF) model proposed by Deco et al. [25], which reduces the activity of large ensembles of interconnected excitatory and inhibitory spiking neurons to a reduced set of dynamical equations describing the activity of coupled excitatory (E) and inhibitory (I) pools of neurons, based on the original reduction of Wong and Wang [79]. In this DMF reduction, the excitatory synaptic currents, $I^{(E)}$,

are mediated by NMDA receptors and the inhibitory currents, $I^{(I)}$, are mediated by GABA_A receptors. Within each brain area n , the E and I neuronal pools are reciprocally connected, whereas inter-area coupling between two areas n and p occurs only at the E-to-E level and is scaled by the structural connectivity C_{np} (see *Methods - Structural Connectivity*).

More specifically, the DMF model at the whole-brain level is expressed by the following system of coupled differential equations:

$$I_n^{(E)} = W_E I_0 + w_+ J_{NMDA} S_n^{(E)} + G J_{NMDA} \sum_p C_{np} S_p^{(E)} - J_n S_n^{(I)}, \quad (1)$$

$$I_n^{(I)} = W_I I_0 + J_{NMDA} S_n^{(E)} - S_n^{(I)}, \quad (2)$$

$$r_n^{(E)} = H^{(E)}\left(I_n^{(E)}\right) = \frac{g_E \left(I_n^{(E)} - I_{thr}^{(E)}\right)}{1 - \exp\left(-d_E g_E \left(I_n^{(E)} - I_{thr}^{(E)}\right)\right)}, \quad (3)$$

$$r_n^{(I)} = H^{(I)}\left(I_n^{(I)}\right) = \frac{g_I \left(I_n^{(I)} - I_{thr}^{(I)}\right)}{1 - \exp\left(-d_I g_I \left(I_n^{(I)} - I_{thr}^{(I)}\right)\right)}, \quad (4)$$

$$\frac{dS_n^{(E)}(t)}{dt} = -\frac{S_n^{(E)}}{\tau_{NMDA}} + \left(1 - S_n^{(E)}\right) \gamma r_n^{(E)} + \sigma v_n(t), \quad (5)$$

$$\frac{dS_n^{(I)}(t)}{dt} = -\frac{S_n^{(I)}}{\tau_{GABA}} + r_n^{(I)} + \sigma v_n(t). \quad (6)$$

Here, for each excitatory (E) or inhibitory (I) pool of neurons in each brain area n , $I_n^{(E,I)}$ (in nA) represents the total input current, $r_n^{(E,I)}$ (in Hz) denotes the firing rate and $S_n^{(E,I)}$ denotes the synaptic gating variable. The neuronal response functions, $H^{(E,I)}$, convert the total input currents received by the E and I pools into firing rates, $r_n^{(E,I)}$, following the input-output function of Abbott and Chance [80], where $g_E = 310 \text{ nC}^{-1}$ and $g_I = 615 \text{ nC}^{-1}$ are gain factors determining the slope of H , $I_{thr}^{(E)} = 0.403 \text{ nA}$, and $I_{thr}^{(I)} = 0.288 \text{ nA}$ are the threshold currents above which the firing rates increase linearly with the input currents, and $d_E = 0.16$ and $d_I = 0.087$ are constants determining the shape of the curvature of H around I_{thr} . The synaptic gating variable of excitatory pools, $S_n^{(E)}$, is controlled by NMDA receptors with a decay time constant $\tau_{NMDA} = 0.1 \text{ s}$ and $\gamma = 0.641$, whereas the average synaptic gating in inhibitory pools depends on GABA receptors with $\tau_{GABA} = 0.01 \text{ s}$. The overall effective external input is $I_0 = 0.382 \text{ nA}$ with $W_E = 1$ and $W_I = 0.7$. Furthermore, $w_+ = 1.4$ is the weight of recurrent excitation and $J_{NMDA} = 0.15 \text{ nA}$ weighs all excitatory synaptic couplings. In Equations 5 and 6 v_n is uncorrelated standard Gaussian noise with an amplitude of $\sigma = 0.01 \text{nA}$. All parameters were set as in Wong and Wang [79].

The parameters of the DMF model were defined in Wong and Wang [79] to emulate resting-state conditions, such that each isolated node displays the typical noisy spontaneous activity with low firing rate ($r^{(E)} \sim 3 \text{Hz}$) observed in electrophysiology experiments [81–84]. Moreover, following Deco et al. [25], the inhibition weight, J_n , was adjusted for each node n such that the firing rate of the excitatory pools $r_n^{(E)}$ remains clamped at 3Hz even when receiving excitatory input from connected areas. This regulation is known as Feedback Inhibition Control (FIC) and the algorithm to achieve it is described in Deco et al. [25]. It has been demonstrated that the FIC leads to a better prediction of the resting-state FC and to a more realistic evoked activity [25].

Following the parcellation applied to the structural and functional MRI data, we considered $N = 90$ brain areas in our whole-brain network model. Each area n receives excitatory input from all structurally connected areas p into its excitatory pool, weighted by the connectivity matrix, C_{np} , obtained from dMRI (see *Methods: Structural Connectivity*). Furthermore, all inter-area E-to-E connections are equally scaled by a global coupling factor G . This global scaling factor is the only control parameter that is adjusted to move the system to its optimal working point, where the simulated activity maximally fits the empirical resting-state activity of participants under placebo conditions.

Simulations were run for a range of G between 0 and 2.5 with an increment of 0.025 and with a time step of 1 ms. For each G , we ran 200 simulations of 435 s each, in order to emulate the empirical resting-state scans from 15 participants.

Simulated BOLD Signal

To transform the simulated mean field activity into a BOLD signal we used the generalized hemodynamic model of Stephan et al. [85]. We compute the BOLD signal in each brain area n from the firing rate of the excitatory pools $r_n^{(E)}$, such that an increase in the firing rate causes an increase in a vasodilatory signal, s_n , that is subject to auto-regulatory feedback. Blood inflow f_n responds in proportion to this signal inducing changes in blood volume v_n and deoxyhemoglobin content q_n . The equations relating these biophysical variables are:

$$ds_n/dt = 0.5r_n^{(E)} + 3 - ks_n - \gamma(f_n - 1) \quad (7)$$

$$df_n/dt = s_n \quad (8)$$

$$\tau dv_n/dt = f_n - v_n^{\alpha^{-1}} \quad (9)$$

$$\tau dq_n/dt = f_n(1 - \rho)^{f_n^{-1}} / \rho - q_n v_n^{\alpha^{-1}} / v_n \quad (10)$$

where ρ is the resting oxygen extraction fraction, τ is a time constant and α that represents the resistance of the veins. Finally, the BOLD signal in each area n , B_n , is a static nonlinear function of volume, v_n , and deoxyhemoglobin content, q_n , that comprises a volume-weighted sum of extra- and intravascular signals:

$$B_n = V_0 \left[k_1(1 - q_n) + k_2 \left(1 - q_n/v_n \right) + k_3(1 - v_n) \right] \quad (11)$$

All biophysical parameters were taken as in Stephan et al. [85]. To concentrate on the frequency range where resting-state activity appears the most functionally relevant, both empirical and simulated BOLD signals were band pass filtered between 0.1 and 0.01 Hz [8, 86–88].

5. Serotonergic Modulation

We used the high-resolution atlas of human brain serotonin system measured with PET by Beliveau et al. [18] (see above) to obtain a quantitative measure of 5-HT_{2A} receptor density in each AAL region n , $d5HT2A_n$. Density values were divided by the maximum, such that $\max(d5HT2A) = 1$.

We used $d5HT2A_n$ to modulate the firing rates $r_i^{(E,I)}$ of the excitatory and inhibitory pools of each brain region, following a number of experimental studies in cats and rats showing that serotonin injection modulates the firing rate of neurons with 5-HT receptors [89–93]. Moreover, while some neurons respond with an increased firing rate, others consistently decrease the firing rate after serotonin injection, indicating that 5-HT_{2A} receptors have both excitatory and inhibitory effects [89, 90].

To be precise, we consider that $d5HT2A_n$ modulates the gain of the neuronal response function $H^{(E)}$ in each brain area according to the modified Equation 3, using the standard computational definition of gain modulation given by Chance and colleagues [94]:

$$r_n^{(E)} = H^{(E)}(I_n^{(E)}) = \frac{g' g_E(I_n^{(E)} - I_{thr}^{(E)})}{1 - \exp(-d_E g' g_E(I_n^{(E)} - I_{thr}^{(E)}))} \quad (12)$$

$$g' = 1 + s_E d5HT2A_n$$

Here, the scaling factor s_E is the only free parameter equally scaling in all brain areas the slope of H in the E pool according to the normalized density of serotonin receptors in each area, $d5HT2A_n$. To simulate the resting-state activity under placebo condition, we use $s_E = 0$.

DATA AND SOFTWARE AVAILABILITY

The code to run the analysis is available on GitHub (<https://github.com/decolab/cb-neuromod>). The multimodal neuroimaging data from the experiment is available upon request.